Journal of Materials Chemistry A

Accepted Manuscript

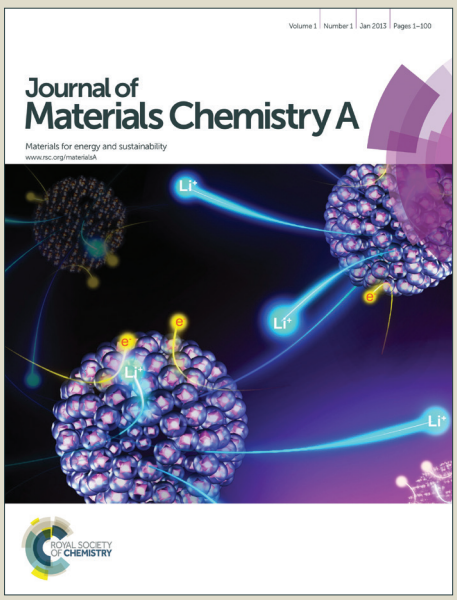

ROYAL SOCIETY OF CHEMISTRY

www.rsc.org/materialsA

A novel monolithic three-dimensional graphene-based composite with enhanced electrochemical performance

Hai-Tao Xu, Ling Fang, Yanping Mu, Hua-Jun Qiu, Yu Wang**

The State Key Laboratory of Mechanical Transmissions and School of Chemistry and Chemical Engineering, Chongqing University, Chongqing 400044, China

*Email: wangy@cqu.edu.cn;

hjqiu@cqu.edu.cn;

Abstract

A monolithic 3D porous graphene with a small pore size of ~250 nm is obtained by a chemical vapor deposition method by using dealloyed nanoporous Ni as substrates. A monolithic nanocomposite of CoO or PdCo nanoparticles decorated on the 3D porous graphene was facilely synthesized and used as an advanced anode material for lithium ion batteries or as electrocatalyst in fuel cells. The synthesized CoO or PdCo alloy nanoparticles with narrow diameter distributions are uniformly anchored on the porous graphene inner surface. The CoO/porous graphene nanocomposite displays a high performance in lithium ion batteries with a large reversible capacity, excellent cycling stability, and good rate performance. The PdCo/porous graphene exhibits an enhanced catalytic activity for the oxidation of ethanol compared with both Pd/porous graphene and commercial Pd/C, highlighting the importance of the monolithic porous graphene on enhancing the electrochemical performance of metal and metal oxide nanoparticles.

Keywords: three-dimensional graphene, PdCo, ethanol oxidation, lithium ion batteries

Introduction

As a green power source, lithium ion batteries (LIBs) have been widely used in modern society and also attracted great research interest due to the importance. So far, various materials such as graphitic/non-graphitic carbon, transition metal oxides and

their composites, etc., have been exploited as the anode materials for LIBs.[1] Among the transition metal oxides, Co_3O_4 and CoO attract much interest for LIBs due to their high theoretical capacity.[2-7] However, the large volume expansion/contraction and severe particle aggregation during the Li insertion/extraction process lead to electrode pulverization and loss of interparticle contact, resulting in a large irreversible capacity loss and poor cycling stability. To solve these intractable problems, various appealing strategies have been developed, including the fabrication of carbon-based nanocomposites and unique Co_3O_4 or CoO nanostructures/microstructures.[2, 8-10] However, to keep large reversible capacity combined with high coulombic efficiency, the fabrication of novel cobalt oxide-based electrode material remains a great challenge.

Graphene, a two-dimensional single-layer sheet of graphite with p-electrons fully delocalized on the graphitic plane, has attracted much attention due to its unique physicochemical properties, such as high surface area, high conductivity and strong mechanical strength.[8-17] Graphene has been exploited as a promising material for energy storage, bioelectronics and electrocatalytic applications.[18-28] For example, Tao *et al*.[28] reported a green and economic strategy to fabricate Pt on nitrogen-doped graphene using a single–step hydrothermal method and further certified its high electrocatalytic activity. In LIBs and electrocatalysis, graphene is often used as a support for active nanoscale materials such as metal or metal oxides to improve their electrochemical performance because the ultrathin flexible graphene can not only work as a highly conductive matrix for enabling good contact but also effectively prevent the volume expansion/contraction and aggregation of NPs during Li charge/discharge process. So far, most works have focused on the use of graphene powder (i.e., reduced graphene oxide, r-GO) as a support because of the low-cost and large-scale production enabled by the chemical exfoliation processes using even industry carbonaceous waste as precursors.[10, 11, 13, 17, 29-31] However, some unique graphene properties are usually severely impaired in r-GO due to the abundant defects and functional moieties created during the synthesis procedures.[32] The aggregation and stacking between individual graphene sheets driven by the strong π-π interaction would result in significant reduction of the graphene intrinsic high specific surface area. Moreover, due to the inter-sheet contact resistance, the conductivity of graphene is largely compromised.

Compared with r-GO powder, the monolithic three-dimensional (3D) porous graphene film by chemical vapor deposition (CVD) method [33-35] is expected to exhibit enhanced property for its applications as supports. However, the pore size of the usually used commercial Ni foam template is very large (several hundred micrometers [36, 37]), resulting in a low volume specific surface area of graphene and consequently a low volumetric loading of active nanomaterials and energy capacity. In order to enhance the volumetric surface area of monolithic porous graphene, the development of porous Ni (or Cu) template with nanoscale pore size is very urgent.

In previous work, using dealloyed nanoporous Ni with a pore size of ~10 nm as a template and catalyst, we have synthesized a monolithic nanotubular porous graphene with small pore/tube sizes of ~250 nm. It has been extensively studied that the graphene can be considered as promising support materials for Pd-based electrocatalysts and electrode material.[38] Due to the importance and multifunction of graphene-based composites, in this work, we decorated the porous graphene with CoO or PdCo alloy nanoparticles (NPs) through a simple solvothermal method. Importantly, the porous graphene networks decorated with CoO and PdCo NPs are demonstrated to be an excellent anode material for LIBs and electrocatalyst for fuel cells, respectively.

Experimental section

Synthesis of 3D porous graphene

Nanoporous Ni with a pore/ligament size of ~10 nm was prepared by dealloying a melt-spinned $Ni_{25}Mn_{75}$ alloy.[39] 3D porous graphene was synthesized by chemical vapor deposition (CVD) using the nanoporous Ni as substrate. The nanoporous Ni placed into a quartz tube was heated at 900°C under 2500 sccm Ar and 100 sccm H_2 for 3 min. After the pre-treatment, benzene (0.5 mbar, 99.8%, anhydrous) was introduced with the gas flow of Ar (2500 sccm) and H_2 (100 sccm) at 900°C for graphene growth. After ~2 min growth, the sample was rapidly cooled to the room temperature under H_2/Ar flow. Finally, the sample was cut into small pieces (1 cm × 1 cm) and the Ni substrate was etched away with HCl (2 M) solution to prepare the flexible porous graphene.

Preparation of CoO (PdCo)/porous graphene composite

The CoO/porous graphene nanocomposite was synthesized in an oil-phase solution. Typically, a black piece of porous graphene was mixed with 0.15 mM $Co(acac)_3$ (acac: acetylacetonate) in 5 mL of oleylamine (OAm), and then heated at 200^{o}C for 2 h. After the reaction, the porous graphene was taken out, washed with ethanol three times, and then annealed at 350^{o}C for 1 h in Ar atmosphere. PdCo alloy NPs decorated porous graphene (PdCo/porous graphene) nanocomposites were synthesized by adding 0.15 mM $Pd(acac)_2$ in the 0.15 mM $Co(acac)_3$ OAm solution. Pd/porous graphene was synthesized in the same solution without $Co(acac)_3$. Both the PdCo/porous graphene and Pd/porous graphene were also annealed at 350^{o}C for 1 h in Ar atmosphere.

Characterization

X-ray diffraction (XRD) analysis was carried out on a Bruker D8 advanced X-ray diffractometer using Co Kα radiation at a step rate of 0.04^{o} s^{-1}. The morphology of the sample was characterized by a JEM-1400 transmission electron microscope (TEM) and a JSM-6700 field-emission scanning electron microscope (SEM) equipped with an Oxford INCA x-sight energy dispersive X-ray spectrometer (EDS).

Carbon content tests

To determine the loading amount of the functional NPs, 100 mg of the samples (CoO/porous graphene and PdCo/porous graphene) were mixed with concentrated nitric acid. After complete dissolution, the porous graphene was collected, washed and dried in an oven at 60°C overnight. The loading amount of the NPs was calculated based on the mass difference before and after the dissolution. The loading of the NPs in CoO/graphene and PdCo/graphene is 83.9 wt% and 85.2 wt%, respectively.

Electrochemical measurements

For half-cell test of the free-standing CoO/porous graphene, coin cells were fabricated. Prior to cell fabrication, the free-standing graphene was heated in a vacuum oven at 80°C for 8 h. Pure Li foil (99.9%, Aldrich) was used as the counter electrode and 1 M $LiPF_6$ in ethylene carbonate and diethyl carbonate (EC-DEC, v/v =

1:1) as electrolyte. Celgard 2400 was used as the separator film to isolate the two electrodes. The coin cell tests were performed without conventional metal current collectors, carbon black and binder. The cell was assembled in an argon-filled glove box where moisture and oxygen concentrations were strictly limited to below 0.1 ppm. The galvanostatic cyclying was performed on Neware Battery Testing System, and electrochemical impedance spectrum (EIS) were collected using electrochemical workstation (CHI 660C).

Electrochemical catalytic tests were performed on a CHI660C workstation in a standard three-electrode cell with a free-standing 3D graphene composite as working electrode, a Pt foil as counter electrode and a saturated calomel electrode (SCE) as reference electrode. The current densities were normalized by the electrochemically active surface areas (EASAs) of the Pd-based electrodes (calculated according to the reduction charge of Pd oxide monolayer).[40] The commercial Pd/C catalyst (10 wt.%) is from Sigma-Aldrich.

Results and discussion

Preparation and characterization of 3D CoO/porous graphene

The pore size of the as-dealloyed nanoporous Ni is ~10 nm. The pore size increases dramatically to ~250 nm after the CVD growth of graphene at high temperature of 900^{o}C. After the dissolution of porous Ni in an acidic solution, the obtained monolithic 3D porous graphene exhibits a black color and flexible property.[34] The mean pore size of the graphene is about 200 nm and the pore-ligament morphology of the porous Ni substrate is well-inherited by the monolithic graphene (Fig. S1). Characterization of the monolithic graphene by Raman spectroscopy (Fig. 1) reveals two characteristic peaks at ~1560 cm^{-1} (G-band) and ~2700 cm^{-1} (2D-band) which are consistent with previously published results.[40] According to the previous works,[41-44] the intensity of G-band (I_G) increases monotonically with the increase of graphene thickness whereas I_{2D} is relatively stable, and I_G/I_{2D} scales linearly with the number of graphene layers (up to 4 layers).[45] In our work, the I_G/I_{2D} ratio of the 3D graphene is 1.6, which indicates that the 3D graphene contains few layers.[46] The D-band (at ~1350 cm^{-1}) is originated from the disordered carbon in graphene, and its intensity

indicates the density of defects in the as-grown graphene film.[47] The extremely weak D-band in the Raman spectra indicates that the obtained monolithic 3D porous graphene is of high quality.

The porous graphene was then used as a support to form a CoO/porous graphene composite with highly loaded CoO NPs by an oil-phase reaction process. The hydrophobic graphene provided a suitable substrate for the nucleation and growth of CoO nanocrystals in OAm. The strong interaction between electron-rich Co atoms and electrophilic C atoms of graphene makes Co and CoO being strongly anchored on the graphene surface during the nucleation and growth process. OAm, serving as both the solvent and the reducing agent, plays a key role in promoting the thermal decomposition of $Co(III)(acac)_3$ to $Co(II)O$[5] and its subsequent homogeneous dispersion on graphene owing to the good hydrophobic interaction between OAm and graphene.[23,48, 49] Fig. 2a shows a representative section-view SEM image of the CoO/porous graphene composite. It can be observed that the CoO NPs are uniformly anchored on the porous nanotubular-like graphene ligament surface. The structure of the nano-composites was also examined by TEM (Fig. 2b). As observed, high density and uniform CoO NPs are homogeneously immobilized on the whole surface of the graphene. The diameter of the CoO NPs ranges from 2 nm to 9 nm (Fig. S2a). The HRTEM image displays clear crystal lattices with d-spacing of 0.21 nm, corresponding to the (200) plane of CoO crystals. The crystal structure of the CoO/porous graphene was further characterized by XRD (Fig. 3). The XRD pattern shows that the positions and relative intensities of all the diffraction peaks match well with standard CoO patterns. The diffraction peaks at the degree of 42.7^{o} (111), 49.7^{o} (200) and 72.9^{o} (220) are consistent with the standard XRD data for cubic CoO (JCPDS Card File No. 78-0431). The peak at $\sim 30.5^{o}$ can be ascribed to graphite, indicating the graphitic nature of 3D porous graphene. Moreover, the chemical composition of the composite was tested by EDS (Fig. 2d). It is shown that C, Co, O elements are the main elements. The signal of Si is from the substrate used for SEM. To evaluate the influence of reaction temperature in the oven on some parameters of the composites, such as the particle size and particle content, the reaction temperature was increased to 220°C. It was found that the loading amount of CoO NPs increased, however, the particle sizes become larger and the particles began to aggregate.

Interestingly, this oil-phase based synthesis strategy can also be used to immobilize noble metal-based alloy NPs on the porous graphene surface. For example, after the addition of some $Pd(acac)_2$ in the $Co(acac)_3$ solution, porous graphene decorated with PdCo NPs (PdCo/porous graphene) is obtained. As shown in the SEM image (Fig. 4a), the PdCo alloy NPs are uniformly distributed on the nanotubular graphene ligament surface. TEM characterization (Fig. 4b) shows that the NPs are around 5 nm in average with a narrow size distribution from 2 to 9 nm (Fig.S2b). The clear lattice fringes in the HRTEM image indicates that the alloy NPs are well crystallized (Fig. 4c). The crystal nature of the alloy NPs is further studied by XRD analysis (Fig. 3). The three diffraction peaks located at 47.1^o, 54.9^o, and 80.9^o can be ascribed to the (111), (200) and (220) diffraction of face-centered-cubic PdCo alloy. Compared with the standard pattern of Pd, the peak positions slightly shift to right, suggesting the incorporation of smaller Co in the NPs. No diffraction peaks from CoO can be observed, indicating that the presence of $Pd(acac)_2$ in the solution can facilitate the reduction of Co(III) to Co and also successfully protect the Co from oxidation during the whole process. EDS analysis (Fig. 4d) shows that the composition of the PdCo alloy is around $Pd_{78}Co_{22}$, which is also tunable to some extent by adjusting the initial contents of the two elements in the solution. In this synthesis, OAm plays a key role for reducing $Co(acac)_3$ and $Pd(acac)_2$ to PdCo alloy NPs and its subsequent uniform dispersion on graphene thanks to the good contact between OAm and graphene. As is known to all, the electrochemical redox potentials of Pd and Co are different. Thus Pd(II) are easier to be reduced than Co(III), the ratio of Pd is clearly higher than Co in the resulting PdCo alloy NPs although the initial ratio between Pd and Co is 1 in the synthesis solution.

Electrochemical measurement

Fig. 5a shows the galvanostatic discharge-charge curves of the CoO/porous graphene at 0.1 A g^{-1} between 0.01 and 3.0 V *vs* Li/Li^+. It is observed that the as-synthesized CoO/porous graphene nanocomposite exhibits a high initial discharge capacity of ~1833 mAh g^{-1}, which is significantly higher than the theoretical capacity of the CoO/porous graphene composite ($C_{theoretical}=C_{CoO}$ × mass percentage of CoO $+C_{graphene}$ × mass percentage of graphene). As previously reported by Poizot *et al.*,[50]

the electrochemical reaction mechanism of Li with transition metal oxides, such as CoO, NiO, mostly involve a conversion reaction as follows:

$MO + 2Li \leftrightarrow Li_2O + M$

According to the literature, the electrochemically driven size confinement of the metal particles is thus believed to enhance their electrochemical activity towards the formation/decomposition of Li_2O. As seen in Fig. 5b, staring from the second cycle, the capacity decreases to ~1363 mAh g^{-1} and the charge/discharge process becomes very stable after even 200 cycles (96% of the capacity from the second cycle retained) with high Coulombic efficiency (~97%), indicating the high specific capacitance and excellent cycling stability of the CoO/porous graphene composite. For comparison, half-cell tests were carried out to compare the electrochemical performance of the CoO/porous graphene prepared at higher temperature. The CoO/graphene fabricated at 220°C displays low capacity and poor cycling ability due to the aggregation of functional particles (Fig. S3). To the best of our knowledge, the stabilized specific capacity (~1300 mAh g^{-1} after second cycle) is considerably higher than most reported values about CoO-based anode materials such as CoO octahedral nanocages (807 mAh g^{-1} at 0.2 C),[51] CoO/graphene composite (640 mAh g^{-1} at 0.1 A g^{-1})[23] and carbon-coated CoO nanocubes (754.5 mA h g^{-1} at 0.1 A g^{-1})[6]. A detailed comparison is shown in Table 1. To further evaluate its cycling stability and rate performance, continuous increase in current density from 0.1 A g^{-1} to 8 A g^{-1} was carried out (Fig. 5c). It is observed that the capacity decreases with the increase of current density. When the current density increased to 8 A g^{-1}, the capacity could still remain at 602 mAh g^{-1}, manifesting the good rate capability of CoO/porous graphene composite. Moreover, when cycled back to 0.1 A g^{-1}, the capacity recovered can reach ~1355 mAh g^{-1}, which further demonstrates the excellent cycling stability of the designed nanocomposite. The high Li storage performance clearly results from the unique structure of the CoO/graphene composite. Firstly, the porous nanotubular graphene network can not only enhance the electronic conductivity (as shown in AC impedance spectrum in Fig. 5d, the porous graphene-based composite exhibits a low charge-transfer resistance) but also prevent the anchored CoO NPs from detachment, aggregation and pulverization. Secondly, the efficient inner space would allow the volume expansion of the functional nanoparticles while retaining the high

conductivity. Thirdly, the nanoporosity is highly favorable for the free diffusion of electrolyte and the exchange rate of lithium ions. In a word, our CoO/graphene composite demonstrates excellent cyclability, high reversible capacity and improved rate capability due to the good points mentioned above.

To demonstrate the potential application of the 3D porous graphene-based composite in fuel cells and/or electrochemical sensors, the electrocatalytic performance of the PdCo/porous graphene has also been evaluated. Fig. 6a shows the cyclic voltammograms (CVs) of PdCo/porous graphene and commercial Pd/C in 1.0 M KOH solution. As observed, both the two catalysts show hydrogen adsorption/desorption between -1.05 and -0.70 V, and reduction peaks of Pd oxides at ~-0.4 V. Compared with Pd/C, the PdCo/porous graphene shows a slightly negatively shifted reduction peak, indicating that the alloy nanoparticle surfaces are more active due to the incorporation of Co. Similar phenomenon has also been observed in our previous work in studying PdCu alloy nanostructures.[53] Fig. 6b shows the CV of PdCo/porous graphene in 1 M KOH solution containing 1 M ethanol with those of Pd/graphene and Pd/C included for comparison. The peak of ethanol oxidation at ~-0.2 V during the positive scan from PdCo/porous graphene is clearly higher than those from Pd/porous graphene and Pd/C, indicating the facile ethanol oxidation on the PdCo/porous graphene surface. Moreover, the peak position is clearly negatively shifted compared with that of pure Pd/porous graphene thanks to the alloying effect from Co. The peak potential of Pd/porous graphene is also higher than that of Pd/C, which may be caused by the bigger particle size of the synthesized Pd NPs on graphene, decreasing the overall catalytic activity. During the negative scan, another oxidation peak at ~-0.4 V appears. The origin of this oxidation peak is still under debate. Normally, it is suggested that the peak in the negative scan is mainly associated with the removal of carbonaceous species not completely oxidized in the positive scan, rather than caused by freshly chemisorbed species.[54] While some argue that the current peak is from the oxidation of fresh ethanol molecules on a reduced Pd surface.[55] Anyway, the higher peak current density from the PdCo/porous graphene catalyst during the negative scan may further suggest its higher catalytic activity. To test the catalytic stability, the time-current curves of the three catalysts at -0.25 V are then recorded (Fig. 6c). It is observed that the PdCo/porous graphene catalyst displays the highest current density, which is in good agreement with the CV study. The

oxidation current is also relatively stable during the 2500s testing time, showing the potential application of the PdCo/porous graphene in direct ethanol fuel cells.

Conclusions

A small pore 3D porous graphene with a pore size of ~250 nm was prepared by a CVD process using dealloyed nanoporous Ni as templates. The free-standing porous graphene was then decorated with high density and uniform CoO or PdCo alloy NPs by a thermal decomposition process in a $Co(acac)_3$ or $Co(acac)_3$ and $Pd(acac)_2$ mixed solution with OAm as both the solvent and the reducing agent. The use of OAm played a key role in attaching CoO NPs uniformly on the monolithic porous graphene surface owing to the hydrophobic property of CVD-grown graphene. When evaluated as anodes for LIBs, the as-prepared CoO/porous graphene composite exhibits a large reversible capacity, excellent cycling stability, and a high rate performance. The robust composite structures, high amount of accessible active sites, and the synergistic effects between CoO NPs and graphene may be responsible for the high performance. Moreover, PdCo alloy NPs/porous graphene displays an enhanced catalytic activity for ethanol oxidation when compared with both Pd/porous graphene and commercial Pd/C catalysts.

Acknowledgements

This work was financially supported by the Thousand Young Talents Program of the Chinese Central Government (Grant No. 0220002102003), National Natural Science Foundation of China (NSFC, Grant No. 21373280, 21403019), the Fundamental Research Funds for the Central Universities (0301005202017), Beijing National Laboratory for Molecular Sciences (BNLMS) and Hundred Talents Program at Chongqing University (Grant No. 0903005203205).

Supporting Information Available: More SEM images, diameter distribution diagrams and electrochemical data are available in the supporting information for this paper.

Reference

1. M. S. Whittingham, *Chem. Rev*, 2004, **104**, 4271.
2. H.-J. Qiu, L. Liu, Y.-P. Mu, H.-J. Zhang and Y. Wang, *Nano Res*, 2014, 1.
3. M. V. Reddy, G. V. Subba Rao and B. V. R. Chowdari, *Chem. Rev*, 2013, **113**, 5364.
4. C. Peng, B. Chen, Y. Qin, S. Yang, C. Li, Y. Zuo, S. Liu and J. Yang, *ACS Nano*, 2012, **6**, 1074.
5. Y. Sun, X. Hu, W. Luo and Y. Huang, *J. Phys. Chem. C*, 2012, **116**, 20794.
6. K. Xie, P. Wu, Y. Zhou, Y. Ye, H. Wang, Y. Tang, Y. Zhou and T. Lu, *ACS Appl. Mater. Interfaces*, 2014, **6**, 10602.
7. C. Zhou, Y. Zhang, Y. Li and J. Liu, *Nano. Lett*, 2013, **13**, 2078.
8. C. Lee, X. D. Wei, J. W. Kysar and J. Hone, *Science*, 2008, **32**1, 385.
9. K. S. Novoselov, A. K. Geim, S. V. Morozov, D. Jiang, Y. Zhang, S. V. Dubonos, I. V. Grigorieva and A. A. Firsov, *Science*, 2004, **306**, 6669.
10. S. Guo and S. Sun, *J. Am. Chem. Soc*, 2012, **134**, 2492.
11. S. Guo, D. Wen, Y. Zhai, S. Dong and E. Wang, *ACS. Nano*, 2010, 4, 3959.
12. J. L. Kang, A. Hirata, H. J. Qiu, L. Y. Chen, X. B. Ge, T. Fujita and M. W. Chen, *Adv. Mater*, 2014, **26**, 269.
13. Y. M. Li, L. H. Tang and J. H. Li, *Electrochem. Commun*, 2009, **11**, 846.
14. R. Kou, Y. Shao, D. Mei, Z. Nie, D. Wang, C. Wang, V. V. Viswanathan, S. Park, I. A. Aksay, Y. Lin, Y. Wang and J. Liu, *J. Am. Chem. Soc*, 2011, **133**, 2541.
15. C. Xu, X. Wang and J. Zhu, *J. Phys. Chem. C*, 2008, **112**, 19841.
16. J. F. Che, L. Y. Shen and Y. H. Xiao, *J. Mater. Chem*, 2010, 20, 1722.
17. X. Guan, J. Nai, Y. Zhang, P. Wang, J. Yang, L. Zheng, J. Zhang and L. Guo, *Chem. Mater*, 2014, **26**, 5958.
18. N. G. Shang, P. Papakonstantinou, P. Wang, S. Ravi and P. Silva, *J. Phys. Chem. C*, 2010, **114**, 15837.
19. K. Jasuja, J. Linn, S. Melton and V. Berry, *J. Phys. Chem. Lett*, 2010, **1**, 1853.
20. H. L. Wang, H. S. Casalongue, Y. Y. Liang and H. J. Dai, *J. Am. Chem. Soc.*, 2010, **132**, 7472.
21. Y. Liu, X. Dong and P. Chen, *Chem. Soc. Rev.*, 2012, **41**, 2283.
22. J.-W. Kim, P. T. Lillehei and C. Park, *J. Mater. Chem*, 2012, **22**, 8408.
23. Y. Qi, H. Zhang, N. Du and D. R. Yang, *J. Mater. Chem. A*, 2013, **1**, 2337.
24. M. Liu, R. Zhang and W. Chen, *Chem. Rev*, 2014, 114, 5117.
25. M. Yu, A. Wang, Y. Wang, C. Li and G. Shi, *Nanoscale*, 2014, **6**, 11419.
26. C. Hu, G. Zheng, F. Zhao, H. Shao, Z. Zhang, N. Chen, L. Jiang and L. Qu, *Energy. Environ. Sci.*, 2014, **7**, 3699.
27. D. Chen, X. Zhao, S. Chen, H. Li, X. Fu, Q. Wu, S. Li, Y. Li, B.-L. Su and R. S. Ruoff, *Carbon*, 2014, **68**, 755.
28. L. Tao, S. Dou, Z. Ma, A. Shen and S. Wang, *Int. J. Hydrogen Energy,*2015, doi:10.1016/j.ijhydene.2015.02.104.
29. Z. S. Wu, W. C. Ren, L. Wen, L. B. Gao, J. P. Zhao, Z. P. Chen, G. M. Zhou, F. Li and H. M. Cheng, *ACS Nano*, 2010, **4**, 3187.
30. G. Q. Zhang, B. Y. Xia, X. Wang and X. W. Lou, *Adv. Mater*, 2014, **26**, 2408.
31. O. Akhavan, K. Bijanzad and A. Mirsepah, *Rsc. Adv*, 2014, **4**, 20441.
32. X. C. Dong, C. Y. Su, W. J. Zhang, J. W. Zhao, Q. D. Ling, W. Huang, P. Chen and L. J. Li, *Phys. Chem. Chem. Phys*, 2010, **12**, 2164.

33. Z. P. Chen, W. C. Ren, L. B. Gao, B. L. Liu, S. F. Pei and H. M. Cheng, *Nat. Mater*, 2011, **10**, 424.
34. Y. Ito, Y. Tanabe, H.-J. Qiu, K. Sugawara, S. Heguri, N. H. Tu, K. K. Huynh, T. Fujita, T. Takahashi, K. Tanigaki and M. W. Chen, *Angew. Chem. Int. Edit.*, 2014, **126**, 4922.
35. H. Qiu, X. Dong, B. Sana, T. Peng, D. Paramelle, P. Chen and S. Lim, *ACS. Appl. Mater. Interfaces*, 2013, **5**, 782.
36. C. Wu, Q. Shen, R. Mi, S. Deng, Y. Shu, H. Wang, J. Liu and H. Yan, *J. Mater. Chem. A*, 2014, **2**, 15987.
37. M. Huang, F. Li, X. L. Zhao, D. Luo, X. Q. You, Y. X. Zhang and G. Li, *Electrochim. Acta*, 2015, **152**, 172.
38. Q. Liu, Z. Wu, Z. Ma, S. Dou, J. Wu, L. Tao, X. Wang, C. Ouyang, A. Shen and S. Wang, *Electrochimica Acta,*2015, doi:10.1016/j.electacta.2015.01.193.
39. J. L. Kang, A. Hirata, H. J. Qiu, L. Y. Chen, X. B. Ge, T. Fujita and M. W. Chen, *Adv. Mater*, 2014, **26**, 269.
40. W. Pan, X. K. Zhang, H. Y. Ma and J. T. Zhang, *J. Phys. Chem. C*, 2008, **112**, 2456.
41. A. C. Ferrari, J. C. Meyer, V. Scardaci, C. Casiraghi, M. Lazzeri, F. Mauri, S. Piscanec, D. Jiang, K. S. Novoselov, S. Roth and A. K. Geim, *Phys. Rev. Lett*, 2006, **97**, 187401.
42. I. Calizo, A. A. Balandin, W. Bao, F. Miao and C. N. Lau, *Nano. Lett*, 2007, **7**, 2645.
43. K. N. Kudin, B. Ozbas, H. C. Schniepp, R. K. Prud'homme, I. A. Aksay and R. Car, *Nano. Lett*, 2008, **8**, 36.
44. K. S. Kim, Y. Zhao, H. Jang, S. Y. Lee, J. M. Kim, K. S. Kim, J. H. Ahn, P. Kim, J. Y. Choi and B. H. Hong, *Nature*, 2009, **457**, 706.
45. O. Akhavan, *Carbon*, 2015, **81**, 158.
46. D. Graf, F. Molitor, K. Ensslin, C. Stampfer, A. Jungen, C. Hierold and L. Wirtz, *Nano Lett*, 2007, **7**, 238.
47. X.C. Dong, H. Xu, X.W. Wang, Y.X. Huang, M.B. Chan-Park, H. Zhang, L.H. Wang, W. Huang, P. Chen, *ACS Nano*, **6**, 3206.
48. S. Dresselhaus, A. Jorio, M. Hofmann, G. Dresselhaus and R. Saito, *Nano. Lett*, 2010, **10**, 751.
49. W. S. Seo, J. H. Shim, S. J. Oh, E. K. Lee, N. H. Hur and J. T. Park, *J. Am. Chem. Soc*, 2005, **127**, 6188.
50. P. Poizot, S. Laruelle, S. Grugeon, L. Dupont and J. M. Tarascon, *Nature*, 2000, **407**, 496.
51. H. Guan, X. Wang, H. Q. Li, C. Y. Zhi, T. Y. Zhai, Y. Bando and D. Golberg, *Chem. Commun*, 2012, **48**, 4878.
52. Y. M. Sun, X. L. Hu, W. Luo and Y. H. Huang, *J. Mater. Chem*, 2012, **22**, 13826.
53. C. X. Xu, A. H. Liu and H. J. Qiu, *Electrochem. Commun*, 2011, **13**, 766.
54. C. C. Qiu, R. Shang, Y. F. Xie, Y. R. Bu, C. Y. Li and H. Y. Ma, *Mater. Chem. Phys*, 2010, **120**, 323.
55. Z. X. Liang, T. S. Zhao, J. B. Xu and L. D. Zhu, *Electrochem. Acta*, 2009, **54**, 2203.
56. W. W. Yuan, J. Zhang, D. Xie, Z. M. Dong, Q. M. Su and G. H. Du, *Electrochem Acta*, 2013, **108**, 506.
57. X. F. Zheng, G. F. Shen, Y. Li, H. N. Duan, X. Y. Yang, S. Z. Huang, H. E. Wang, C. Wang, Z. Deng and B. L. Su, *J. Mater. Chem. A*, 2013, **1**, 1394.

58. J. Jiang, J. P. Liu, R. M. Ding, X. X. Ji, Y. Y. Hu, X. Li, A. Z. Hu, F. Wu, Z. H. Zhu and X. T. Huang, *J. Phys. Chem. C*, 2010, **114**, 929.

Figure captions:

Fig. 1 Raman spectrum of the 3D porous graphene.

Fig. 2 SEM (a), TEM (b), HRTEM (c) and EDS spectrum images (d) of the CoO nanoporous graphene composite.

Fig. 3 XRD patterns of the CoO NPs/porous graphene and PdCo/porous graphene composites (the green and blue curves refer to the standard XRD data of Pd and Co.

Fig. 4 SEM (a), TEM (b), HRTEM (c) and EDS spectrum images (d) of the PdCo alloy NPs/porous graphene composite.

Fig. 5 Galvanostatic measurement within the voltage window of 0.01−3.0 V at a rate of 0.1 A g^{-1} (a). Cycling performance of the CoO/porous graphene nanocomposite at 0.1 A g^{-1} (b). Rate-capability test of the CoO/porous graphene nanocomposite (c). AC impedance spectra of CoO/porous graphene electrode (d).The inset shows the magnified spectra in low frequency.

Fig. 6 CV curves of the PdCo/porous graphene and Pd/C in 1 M KOH aqueous solution (a). CV (b) and I-t (c) curves of the PdCo/porous graphene, Pd/porous graphene, and Pd/C in 1 M ethanol + 1 M KOH solution. Scan rate: 20 mV s^{-1}.

Fig. 1

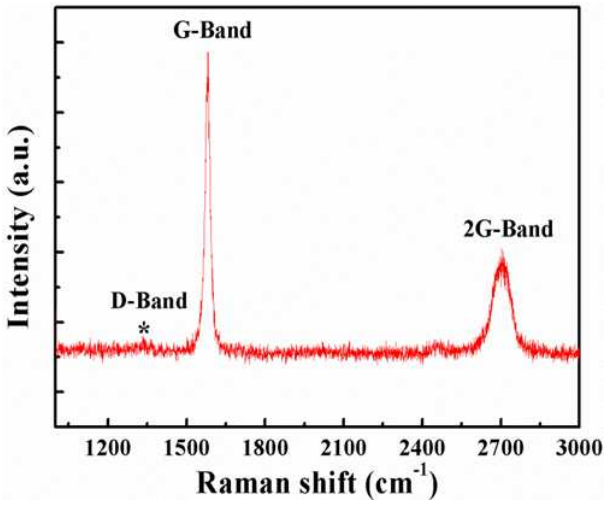

Fig. 2

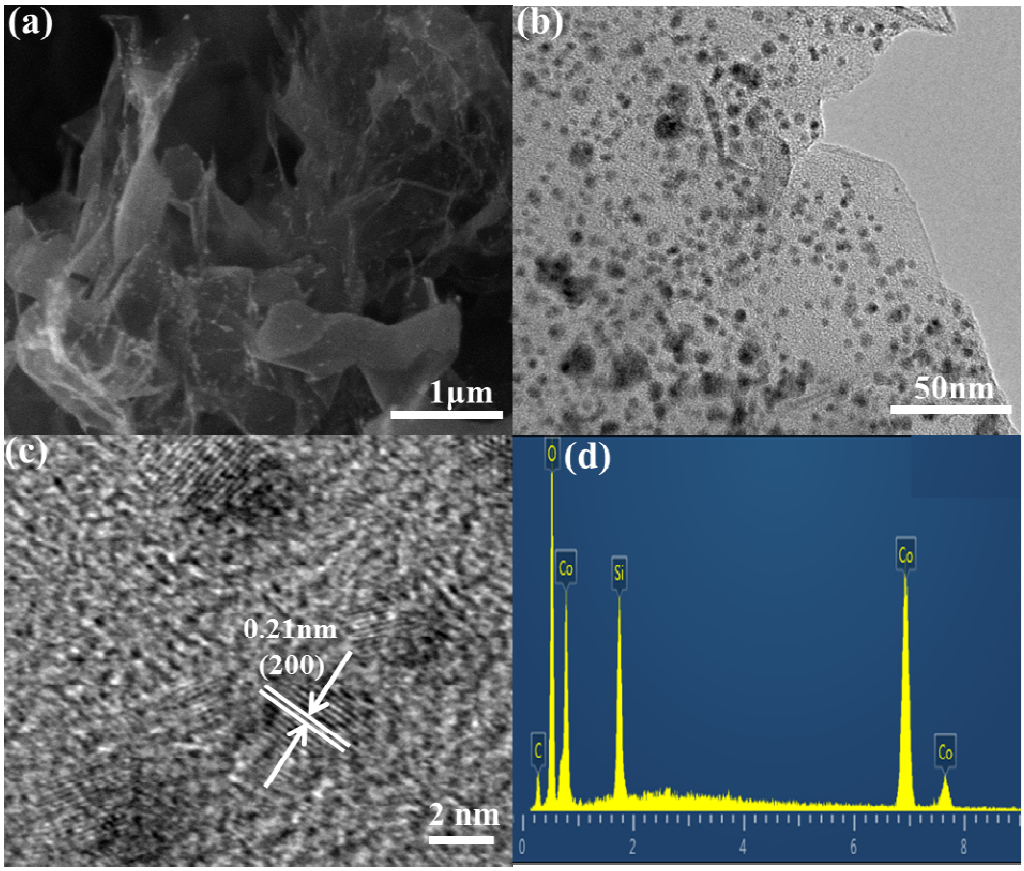

Fig. 3

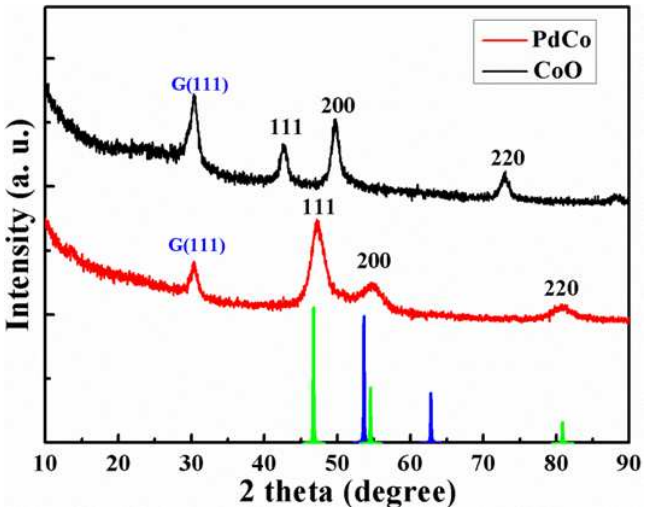

Fig. 4

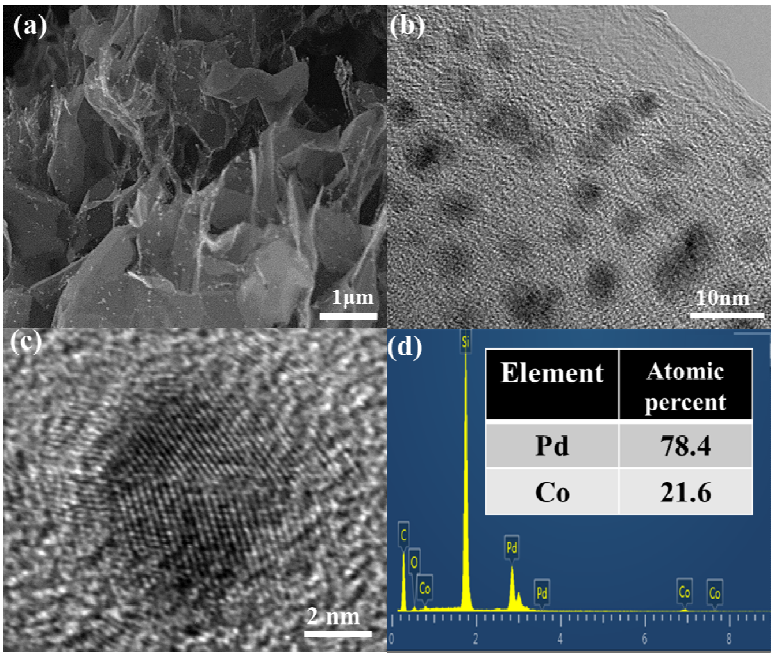

Fig. 5

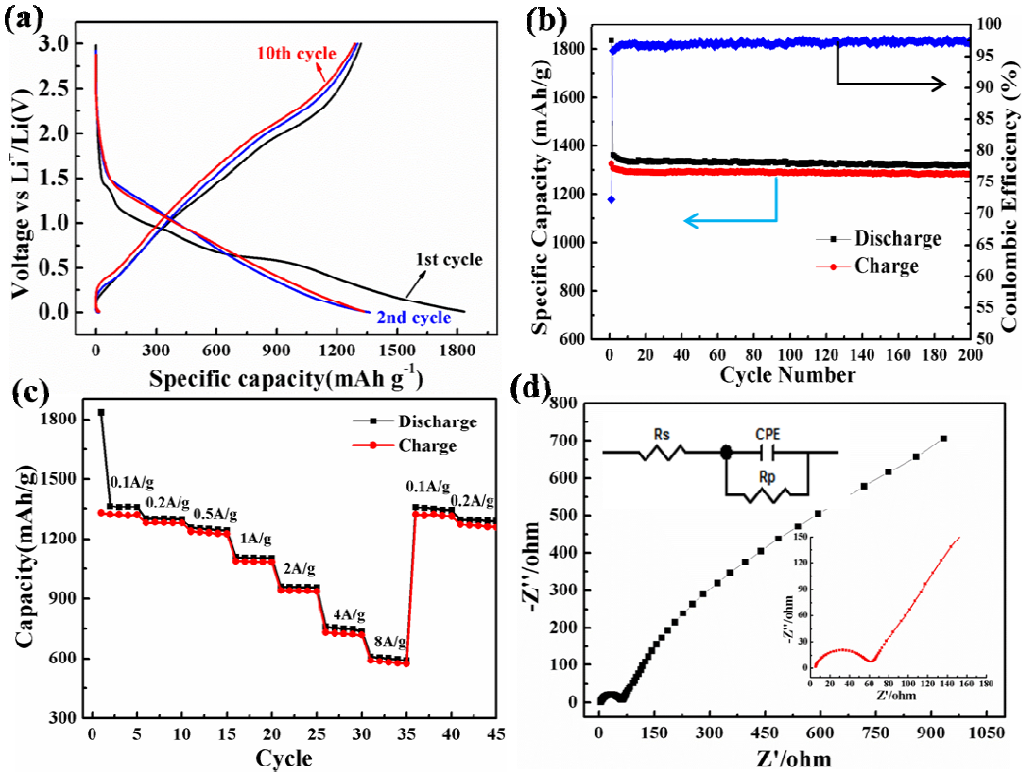

Fig. 6

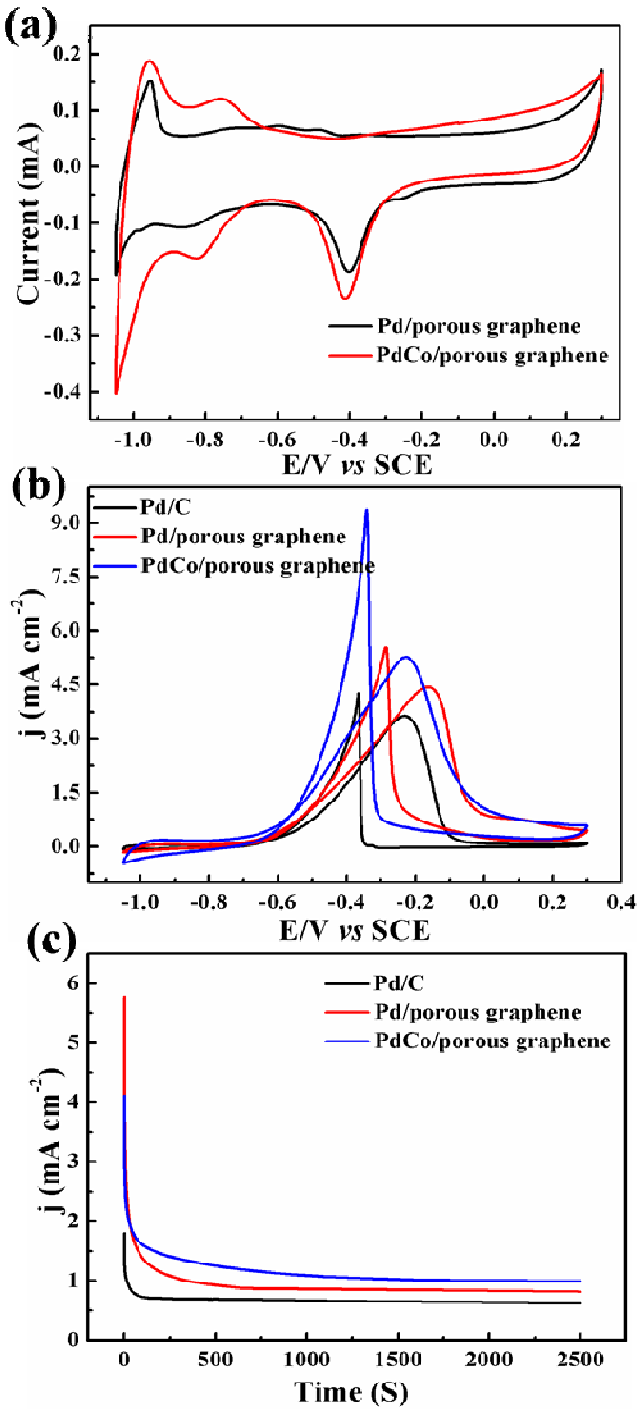

Table 1 Previous reported CoO anode materials for Li-ion battery

Sample	Current density	Stable capacity	Ref.
CoO/porous graphene composites	100 mA g^{-1}	1361 mA h g^{-1}	this work
CoO dot/graphene nanosheet	50 mA g^{-1}	1592 mA h g^{-1}	[4]
CoO nanocubes	100 mA g^{-1}	598.3 mA h g^{-1}	[6]
CoO/graphene nanocomposite	100 mA g^{-1}	1401 mA h g^{-1}	[23]
CoO octahedral nanocages	0.2 C	807 mA h g^{-1}	[51]
CoO nanodisks	200 mA g^{-1}	1118.6 mA h g^{-1}	[52]
CoO/C polyhedra	100 mA g^{-1}	510 mA h g^{-1}	[56]
Microporous CoO nanoparticles	0.2 C	936.2 mA h g^{-1}	[57]
CoO nanowire arrays	1 C	670 mA h g^{-1}	[58]

Table of contents

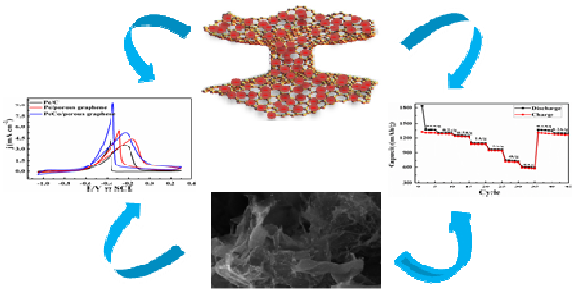

A monolithic nanocomposite of CoO or PdCo nanoparticles decorated on the 3D porous graphene was facilely synthesized and used as an advanced anode material or as electrocatalyst in fuel cells.